Features of the rhombohedral-to-orthorhombic structural phase transition in $La_{1-x}Sr_xMnO_3$

M. Arao and Y. Koyama

Kagami Memorial Laboratory for Materials Science and Technology, Waseda University, 2-8-26 Nishi-Waseda,
Shinjuku-ku, Tokyo 169-0051, Japan
and Department of Materials Science and Engineering, Waseda University, 3-4-1 Okubo, Shinjuku-ku, Tokyo 169-8555, Japan

Y. Inoue

Structural Analysis Section, Research Department, Nissan ARC, Ltd., 1 Natushima-cho, Yokosuka, Kanagawa 237-0061, Japan

Y. Moritomo

Center for Integrated Research in Science and Engineering, Nagoya University, Nagoya 464-8601, Japan
and Precursory Research for Embryonic Science and Technology, Japan Science and Technology Corporation, Nagoya, Japan

The $R\bar{3}c$-to-*Pbnm* structural phase transition in $La_{1-x}Sr_xMnO_3$, which is characterized by changes in the rotational displacement of the MnO_6 octahedra and in the crystal system, has been investigated by transmission electron microscopy. The experimental data indicate that the former change results in the appearance of the antiphase boundary and the latter produces the {110} and {112} twin structures. In addition, the structural phase transition can be reproduced on the basis of the Landau theory, in which a normal structure and an order parameter are, respectively, assumed to be the $Pm3m$ structure and normal coordinates of the rotational displacements.

I. INTRODUCTION

The $R\bar{3}c$-to-*Pbnm* phase transition is one of the common phenomena in $La_{1-x}Sr_xMO_3$ with M = Ti, V, and Mn.[1–3] A crystallographic feature of the $R\bar{3}c$ and *Pbnm* structures is that these structures are produced by introducing a rotational displacement of the MO_6 octahedra into the normal $Pm3m$ structure.[1] According to our previous studies, the rotational displacement involved in the orthorhombic *Pbnm* structure is specified by a $R_{25}^x + R_{25}^y + M_3^z$ displacement, while only the R_{25} displacement, $R_{25}^x + R_{25}^y + R_{25}^z$, occurs in the rhombohedral $R\bar{3}c$ structure.[1,2] The suffixes x, y, and z denote the [100], [010], and [001] directions as the rotation axis, respectively. The rotational directions of two neighboring octahedra along the rotation axis are opposite in the R_{25} displacement and the same in the M_3 one. The $R\bar{3}c$-to-*Pbnm* transition is thus characterized by the change in the rotational displacement from the R_{25} displacement to the M_3 one along the z axis, in addition to that in the crystal system from rhombohedral to orthorhombic. It should be noted that the rotational displacement leads to a decrease in the M-O-M bond angle, resulting in that in the bandwidth, as pointed out in the case of $LaNiO_3$.[4] An examination of the $R\bar{3}c$-to-*Pbnm* structural phase transition is thus needed for a proper understanding of the physical properties of $La_{1-x}Sr_xMnO_3$.

In $La_{1-x}Sr_xMnO_3$, when the Sr content x increases at room temperature, the structural phase transition occurs around $x=0.17$.[3] Note that the insulating state in $LaMnO_3$ changes into the metallic state around $x=0.16$ at room temperature as a result of increasing the Sr content x. This would seem to suggest that the structural phase transition acts as a trigger of the metal-insulator transition. Another interesting feature of the structural transition in $La_{1-x}Sr_xMnO_3$ is that when the Sr content increases the transition temperature rapidly drops around $x=0.17$ just after crossing the Curie temperature T_c. With Sr content of $x=0.17$, the *Pbnm* phase following the structural transition upon cooling goes back to the $R\bar{3}c$ one under the application of an external magnetic field.[5,6] The magnetic field works to enhance the stability of the $R\bar{3}c$ phase. In order to understand the effect of the magnetic field on the structural phase transition, it is necessary to elucidate the crystallographic features involved. In the present work, we investigated the features of the structural phase transition in $La_{1-x}Sr_xMnO_3$ with $x=0.175$ by transmission electron microscopy. In addition, we discuss the structural phase transition on the basis of the Landau theory, which is consistent with the symmetry requirement. The role of the magnetic field is also considered theoretically.

II. EXPERIMENTAL PROCEDURE

A $La_{1-x}Sr_xMnO_3$ single crystal with $x=0.175$ and grown by the floating-zone method was used in this work to examine the $R\bar{3}c$-to-*Pbnm* structural transition. Its transition temperature was determined to be about 180 K by x-ray powder diffraction and its physical properties were already reported by Urushibara *et al.*[3] Specimens for transmission-electron-microscopy observation were thin films obtained by the crashing and Ar-ion thinning techniques. In order to examine the crystallographic features of the structural phase transition in these samples, *in situ* observation of the phase transition was performed by means of H-800 and H-8100A transmission electron microscopes with the help of a cooling holder.
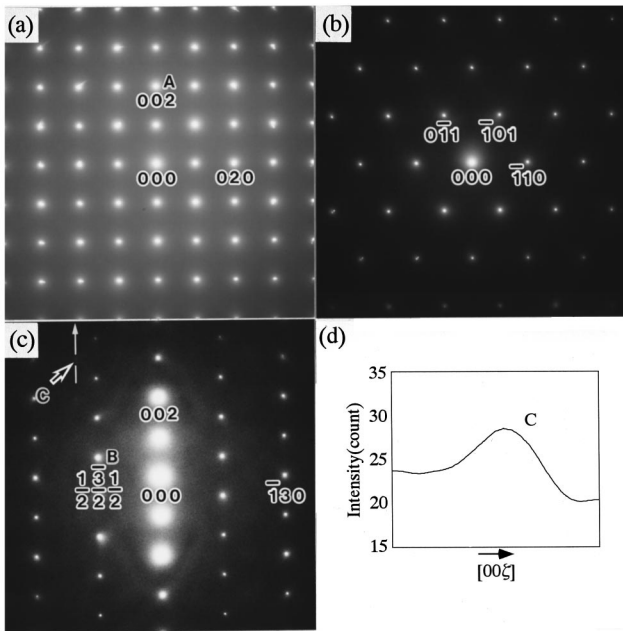
FIG. 1. Electron-diffraction pattern, (a), (b), and (c), taken from $La_{0.825}Sr_{0.175}MnO_3$ sample at room temperature. Electron incidences are parallel to the [100] (a), [111] (b), and [310] (c) directions, respectively. In (d), an intensity profile of diffuse scattering C along a white line in (c) is also shown.

Imaging plates were also used as recording media to avoid sample drift during exposure, in addition to conventional films.

III. RESULTS

Figure 1 shows electron-diffraction patterns taken from the $x = 0.175$ sample at room temperature. Electron incidences in Figs. 1(a)–1(c) are, respectively, parallel to the [100], [111], and [310] directions, and diffraction spots are indexed in terms of the cubic perovskite structure with the space group $Pm3m$. In the electron-diffraction patterns, there are diffraction spots with strong intensities. Since the pseudocubic lattice was adopted for the index, the spots are divided into two groups. The spots in one group are fundamental spots, denoted as A, with an integer index, which are due to the simple perovskite structure of cubic symmetry. The spots in the other group are located at $q = \frac{1}{2}\langle 111 \rangle$ in the cubic reciprocal lattice, as indicated by B. From the extinction rule of the $q = \frac{1}{2}\langle 111 \rangle$ spot, the crystal structure at room temperature was confirmed to be the $R\bar{3}c$ structure, which is characterized only by the R_{25} displacement. In addition, diffuse scattering exists at symmetry-related sites, as indicated by the arrow C. In order to easily detect the presence of the scattering, an intensity profile of diffuse scattering C along a white line in the pattern (c) is shown in Fig. 1(d). The profile clearly shows a broad peak C. The intensity distributions of diffuse scattering in reciprocal space were then measured. It was found that scattering exists around $q = \frac{1}{2}\langle 110 \rangle$ and $q = \frac{1}{2}\langle 100 \rangle$ and has a spherical distribution with a spread of about $\frac{2}{7}G_{001}$, where G_{001} denotes the magnitude of the 001 reciprocal-lattice vector. That is, the diffuse scattering observed in the pattern (c) is a cross section of the diffuse scattering at $q = \frac{1}{2}\langle 100 \rangle$ by the Ewald sphere. Since diffrac-
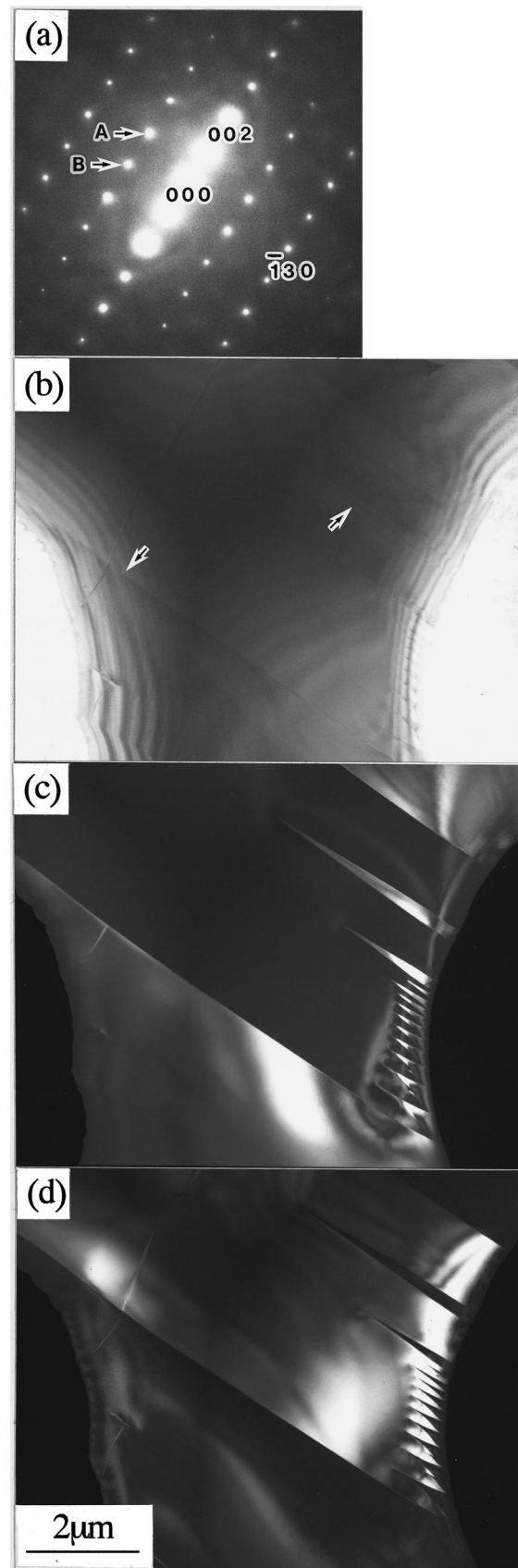

FIG. 2. Electron-diffraction pattern (a), a bright field image (b), and two dark field images, (c) and (d), of $La_{0.825}Sr_{0.175}MnO_3$ sample at room temperature. The electron incidence is parallel to the [310] direction. The dark field images in (c) and (d) were taken by using the $\frac{1}{2}\frac{\bar{3}1}{22}$ and $\frac{1\bar{3}}{22}\frac{\bar{1}}{2}$ spots, marked A and B in the pattern, respectively.

tion spots exhibiting the M_3 rotational displacement appear at $q = \frac{1}{2}\langle 110 \rangle$ and $q = \frac{1}{2}\langle 100 \rangle$ in the *Pbnm* structure, diffuse scattering is an indication that fluctuation occurs in the M_3 displacement in the $R\bar{3}c$ structure. From the spread of the intensity distribution, the coherent length of the fluctuation was determined to be $\frac{7}{2}d_{001} \approx 14$ Å.

La$_{0.825}$Sr$_{0.175}$MnO$_3$ exhibits the $R\bar{3}c$-to-*Pbnm* structural phase transition around 180 K. Figure 2 shows bright and dark field images of the $x = 0.175$ sample at room temperature, together with a corresponding electron-diffraction pattern. The electron incidence is almost parallel to the [310] direction. In the diffraction pattern in Fig. 2(a), there are diffraction spots at $q = \frac{1}{2}\langle 111 \rangle$, in addition to the fundamental spots due to the cubic perovskite structure, as was seen in Fig. 1. There is no conspicuous contrast in the bright field image in Fig. 2(b). Only a line contrast is detected, as indicated by the arrows. We then took dark field images in order to elucidate the domain structure in the $R\bar{3}c$ phase. Figures 2(c) and 2(d) are, respectively, dark field images taken by the $\frac{1}{2}\frac{\bar{3}}{2}\frac{1}{2}$ and $\frac{1}{2}\frac{\bar{3}}{2}\frac{\bar{1}}{2}$ spots, which are marked A and B in the pattern. In Fig. 2(c), a banded region with a width of about 5 μm is seen as a dark contrast. An important feature is that the contrasts in Figs. 2(c) and 2(d) are reversed, indicating that the microstructure of the $R\bar{3}c$ phase is a twin structure consisting of different $R\bar{3}c$ variants. A twin plane was determined to be parallel to the (001) one. That is, the line contrast in Fig. 2(b) is identified as a twin boundary. It is obvious that the {100} twin structure is a consequence of the $Pm3m$-to-$R\bar{3}c$ structural transition, which should occur at a higher temperature.

When the $x = 0.175$ sample was cooled from room temperature, the structural transition to the *Pbnm* phase actually took place around 180 K. Electron-diffraction patterns obtained at 85 K after the transition are shown in Fig. 3. Electron incidences in Figs. 3(a) and 3(b) are, respectively, parallel to the [111] and [310] directions. In the patterns, new diffraction spots appear in the structural phase transition, as indicated by arrows A and B. In addition, a weak diffraction spot, marked by C, is also observed. An intensity profile of spot C along a white line in the pattern (b) is shown in Fig. 3(c), in order to clearly demonstrate the presence of it. Spot A was found to exist at $q = \frac{1}{2}\langle 110 \rangle$ in the simple cubic Brillouin zone, while spots B and C were both at $q = \frac{1}{2}\langle 100 \rangle$. It should be mentioned that spot C was produced by the conversion of diffuse scattering, which was observed in the pattern in Fig. 1(c). We examined the extinction rule of the new spots as well as the $q = \frac{1}{2}\langle 111 \rangle$ spots at 85 K. It was found that the rule for the half integer spots is entirely consistent with the $R_{25}^x + R_{25}^y + M_3^z$ rotational displacement. Thus the crystal structure at 85 K was confirmed to be the *Pbnm* structure.

The domain structure in the *Pbnm* phase was examined by taking dark field images using the $q = \frac{1}{2}\langle 110 \rangle$ spots, which characterize the *Pbnm* structure. Figure 4 shows three dark field images of the $x = 0.175$ sample, a corresponding electron-diffraction pattern, and an intensity profile at 85 K. The electron incidence is almost parallel to the [111] direction. In the pattern in Fig. 4(a), there are three types of spots, $q = \frac{1}{2}[110]$, $q = \frac{1}{2}[101]$, and $q = \frac{1}{2}[011]$, in addition to fun-
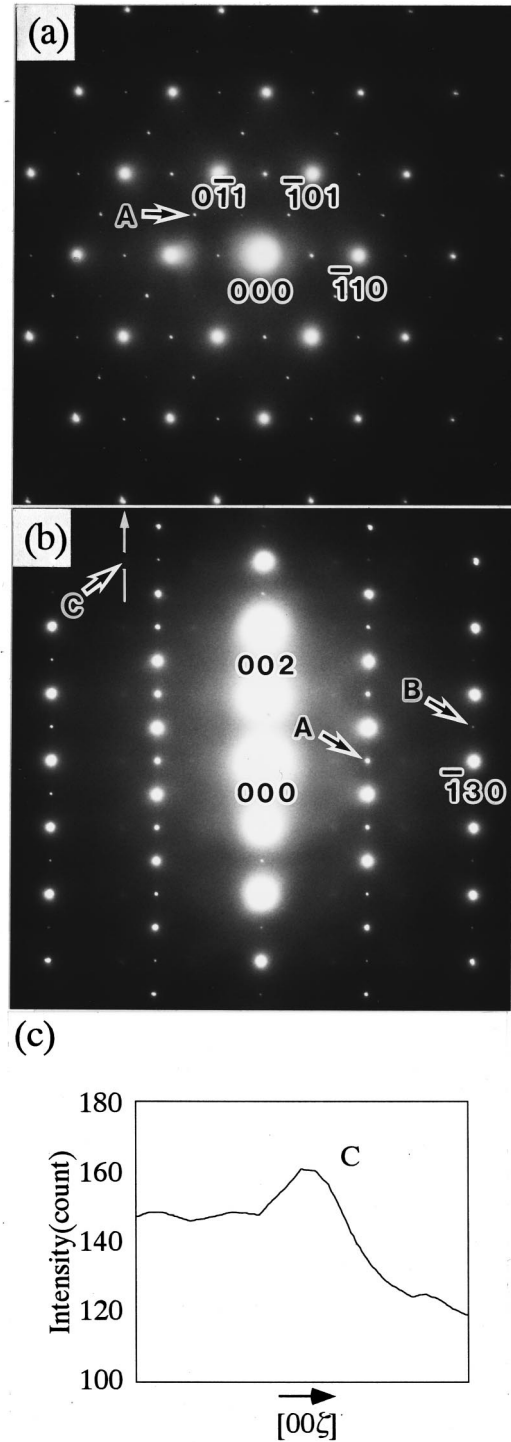

FIG. 3. Electron-diffraction patterns, (a) and (b), of La$_{0.825}$Sr$_{0.175}$MnO$_3$ sample at 85 K. Electron incident beams are parallel to the [111] (a) and [310] (b) directions, respectively. In (c), an intensity profile of diffraction spot C along a white line in (b) is also shown.

damental spots. As the spots at $q = \frac{1}{2}[011]$ are not well reproduced in the pattern, intensity profiles of the $0\frac{1}{2}\frac{1}{2}$ and $0\frac{\bar{1}}{2}\frac{1}{2}$ spots are shown in Fig. 4(b). These peaks are clearly seen in the profile. We took dark field images of Figs. 4(c), 4(d), and 4(e), respectively, using the $\frac{\bar{1}}{2}\frac{1}{2}0$, $\frac{\bar{1}}{2}0\frac{1}{2}$, and $0\frac{\bar{1}}{2}\frac{1}{2}$ spots, which are marked A, B, and C in the pattern. There
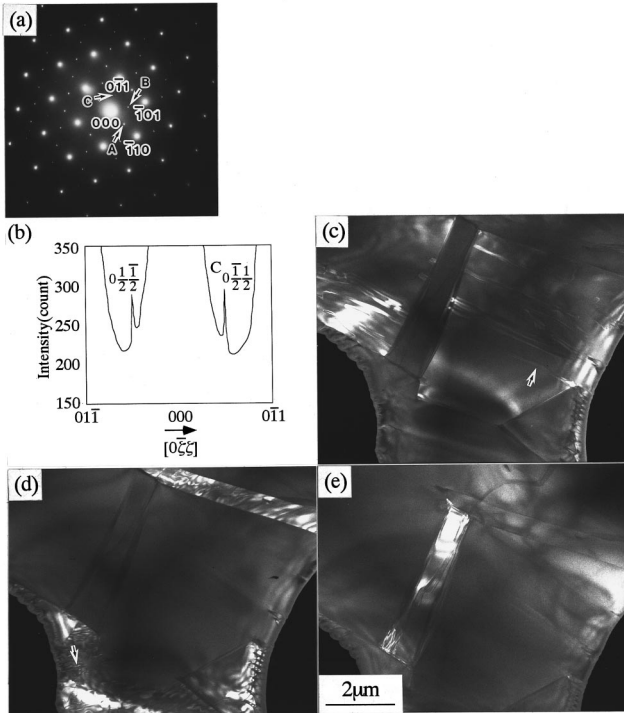
FIG. 4. Electron-diffraction pattern (a), intensity profile (b), and three dark field images, (c), (d), and (e), of $La_{0.825}Sr_{0.175}MnO_3$ sample at 85 K. The electron incidence is parallel to the [111] direction. In (c), an intensity profile of the $0\frac{1}{2}\frac{\bar{1}}{2}$ and $0\frac{\bar{1}}{2}\frac{1}{2}$ spots along the $[0\bar{1}1]$ direction through the origin is shown. The dark field images in (c), (d), and (e), were taken by using the $\frac{\bar{1}}{2}\frac{1}{2}0$, $\frac{\bar{1}}{2}0\frac{1}{2}$, and $0\frac{\bar{1}}{2}\frac{1}{2}$ spots, marked A, B, and C in the pattern, respectively.

exist bright- and dark-contrast regions in these images. In the bright-contrast region, a line contrast is also seen, as indicated by the arrows. A simple analysis of the images indicated that the boundary between the bright- and dark-contrast regions is parallel to the {110} or {112} plane and the line contrast is perpendicular to the ⟨100⟩ direction. It should be noted that the bright-contrast region in each image corresponds to one variant of the *Pbnm* structure because of diffraction contrast. In addition, the line contrast observed in each variant is understood to be an antiphase boundary with respect to the M_3 rotational displacement and to be precisely perpendicular to the [001] direction of the M_3 rotational axis. It is obvious that the appearance of the antiphase boundary results from the change in the rotational displacement in the transition. Figure 5 is a schematic diagram showing the domain structure of the *Pbnm* phase. This diagram was obtained by analyzing the dark field images in Figs. 4. The M_3 rotational axis in each variant is depicted by a double arrow. As is understood from Fig. 5, the domain structure is just a twin structure consisting of three *Pbnm* variants with a different M_3 rotational axis. That is, the change in the crystal system in the transition produces the {110} and {112} twin structures.

Figure 6 shows three electron-diffraction patterns at 85 K, which were taken from a single *Pbnm* variant. The electron incidences in Figs. 6(a), 6(b), and 6(c) are, respectively, parallel to the [100], [110], and [111] directions. In addition to fundamental spots with an integer index, there are diffraction
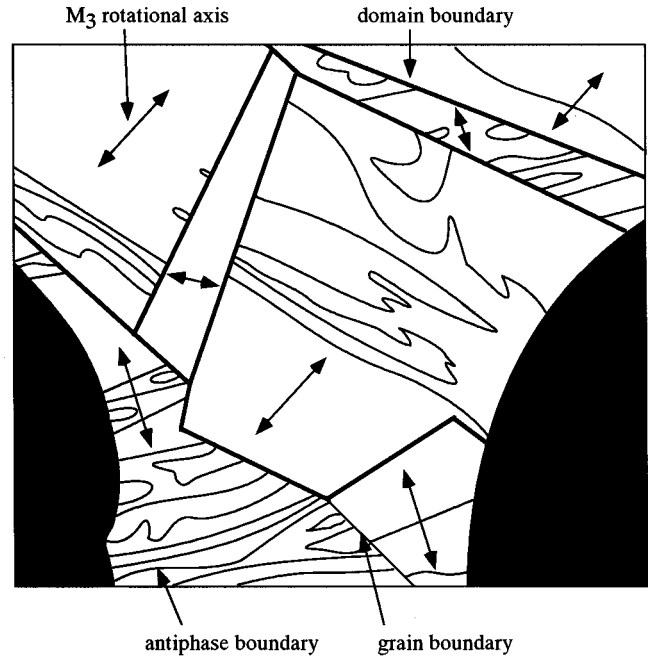

FIG. 5. Schematic diagram of the domain structure of the *Pbnm* phase, obtained by analyzing the dark field images in Figs. 4.

spots at $q=\frac{1}{2}\langle 111\rangle$, $q=\frac{1}{2}\langle 110\rangle$, and $q=\frac{1}{2}\langle 100\rangle$ in the patterns. Among the $q=\frac{1}{2}\langle 110\rangle$ spots, the M_3 rotational displacement involved in the *Pbnm* structure gives rise to the $\frac{1}{2}\frac{1}{2}0$-type spots. Neither a diffraction spot nor diffuse scattering is detected around the other $\frac{1}{2}0\frac{1}{2}$- and $0\frac{1}{2}\frac{1}{2}$-type positions. This originates from the fact that the M_3 mode is one of the nondegenerate phonon modes. In addition, electron diffraction did not reveal any structural fluctuation associated with the Jahn-Teller distortion that has been recently detected by pulsed neutron diffraction.[7]

Figure 7 is a bright field image at room temperature, which was obtained from the $x=0.175$ sample after the reverse transition. Features of the image are found to be the same as those in Fig. 2. This implies that crystallographic reversibility is basically maintained in the normal and subsequent reverse transitions. It is worth noting that the thermal hysteresis of the structural transition was determined to be about 20 K.

IV. DISCUSSION

A. Features of the structural phase transition

The present experimental data clearly show that the changes in the rotational displacement and in the crystal system in the $R\bar{3}c$-to-*Pbnm* structural phase transition result in the appearance of the antiphase boundary perpendicular to the M_3 rotational axis and the twin structures composed of different *Pbnm* variants, respectively. In addition, in spite of the first-order transition, crystallographic reversibility is basically maintained in the normal and subsequent reverse transitions. Because the space group of the *Pbnm* structure is not a subgroup of that of the $R\bar{3}c$ structure, reversibility is not related to the change in the symmetry but originates from a strain field produced in the transition. First, we will discuss the domain structure in the *Pbnm* phase.
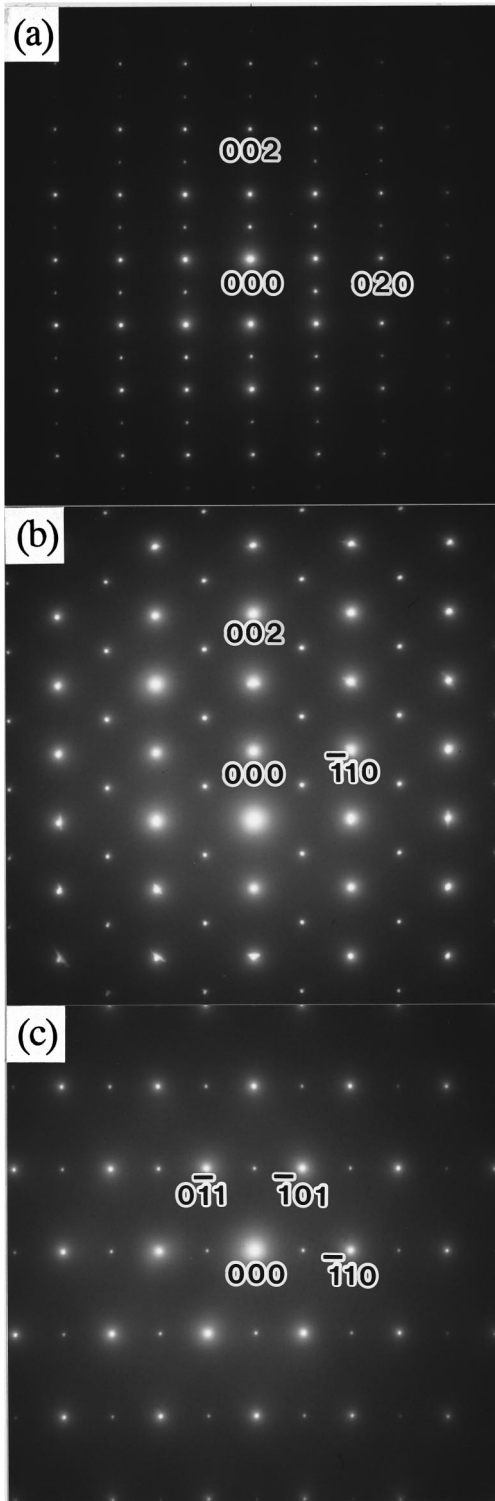
FIG. 6. Electron-diffraction patterns at 85 K, which were taken from a single *Pbnm* variant. Electron incident beams are parallel to the [100] (a), [110] (b), and [111] (c) directions, respectively.

The microstructure of the *Pbnm* phase was found to be the {110} and {112} twin structures. Here, we analyzed the twin structures from the viewpoint proposed by Sapriel.[8] It is obvious that the twin structures originate from the change in the crystal system from rhombohedral to orthorhombic. This change can be regarded as shear deformation. The strain tensors expressing this shear deformation are written as
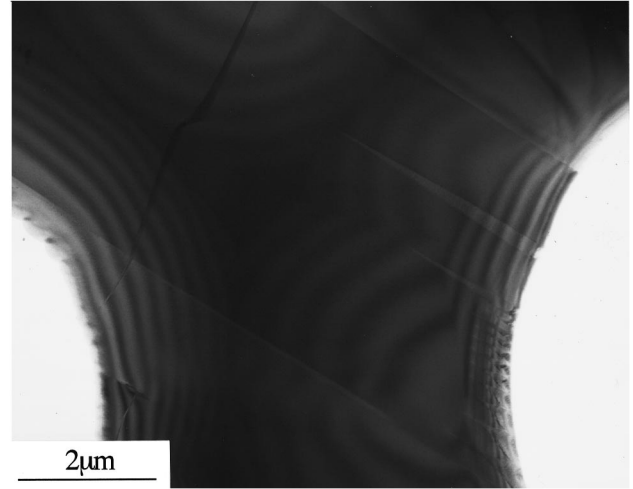

FIG. 7. Bright field image from $La_{0.825}Sr_{0.175}MnO_3$ sample taken at room temperature after the normal and subsequent reverse transitions. The electron incidence is parallel to the [310] direction.

$$S_1 = \begin{pmatrix} 0 & \varepsilon & 0 \\ \varepsilon & 0 & 0 \\ 0 & 0 & 0 \end{pmatrix}, \quad S_2 = \begin{pmatrix} 0 & 0 & 0 \\ 0 & 0 & \varepsilon \\ 0 & \varepsilon & 0 \end{pmatrix}, \quad S_3 = \begin{pmatrix} 0 & 0 & \varepsilon \\ 0 & 0 & 0 \\ \varepsilon & 0 & 0 \end{pmatrix}$$

in the orthorhombic coordinate system. According to Sapriel's theory, when two tensors S_α and S_β are given, the domain walls between S_α and S_β are obtained by $S_\alpha x_i x_j = S_\beta x_i x_j$. For instance, we get $2\varepsilon xy = 2\varepsilon yz$ for S_1 and S_2. Solutions of this simple equation are $y=0$ and $x-z=0$, which lead to the (010) and ($10\bar{1}$) walls in the orthorhombic coordinate system, respectively. We then have the (110) and (112) walls in the cubic coordinate system. The same calculation was made for the other combinations of the strain tensors. As a result, present discussion was found to predict only the {110} and {112} twin planes. This prediction can actually explain the observed domain structure, which is schematically depicted in Fig. 5. It is therefore understood that the crystal-system change in the $R\bar{3}c$-to-*Pbnm* transition takes place via shear deformation.

In the single *Pbnm* variant, there exists the antiphase boundary with a phase slip of $2\pi/2$. The appearance of the antiphase boundary is closely related to the change in the rotational displacement. Here let us consider why the antiphase boundary appears in the transition. In the M_3 rotational displacement, there are two rotational directions; clockwise and counterclockwise. In the transition, regions with these rotations should be nucleated with equal probability. The nucleated *Pbnm* regions then grow and the two regions meet each other. If the two regions are rotating in the same direction, they become one region. Nevertheless, the antiphase boundary appears between the two regions. That is, the emergence of the antiphase boundary is direct proof of the fact that the transition involves changes in rotational displacement.

B. Landau free energy of the $R\bar{3}c$-to-*Pbnm* structural transition

In this section, we propose the Landau-free energy for the $R\bar{3}c$-to-*Pbnm* structural phase transition. The structural

phase transition was already discussed on the basis of the Landau theory.[6] A serious problem with previous discussion is that it does not satisfy the symmetry requirement. That is, the space group of the *Pbnm* structure is not a subgroup of that of the $R\bar{3}c$ structure. Since we must look for a normal structure first, attention is paid to the fact that the $R\bar{3}c$ structure exhibits the {100} twin structure. As was mentioned earlier, the {100} twin structure is the result of the *Pm3m*-to-$R\bar{3}c$ structural transition. In addition, the space groups of the *Pbnm* and $R\bar{3}c$ structures are obviously subgroups of *Pm3m*. Thus we regard the *Pm3m* structure as the normal structure in the transition. As for the main order parameter, there are two candidates: the rotational displacement and the spontaneous strain related to the change in the crystal system. Because the transition should be a staggered one induced by the size effect, the main order parameter is assumed here to be the rotational displacement.

The $R\bar{3}c$ and *Pbnm* structures are, respectively, characterized by the $R_{25}^x + R_{25}^y + R_{25}^z$ and $R_{25}^x + R_{25}^y + M_3^z$ rotational displacement. These displacements are understood to result from the condensation of the triply degenerate R_{25} and nondegenerate M_3 phonon modes in the *Pm3m* structure. That is, the $R\bar{3}c$ and *Pbnm* structures are associated with the three-dimensional R_{25} and one-dimensional M_3 irreducible representations of the space group *Pm3m*. Using the normal coordinates of the R_{25} and M_3 displacements, the free energy can be expressed as

$$F = F_0 + \frac{1}{2}A(T - T_R^*)(Q_{Rx}^2 + Q_{Ry}^2 + Q_{Rz}^2) + \frac{1}{4}B(Q_{Rx}^2 + Q_{Ry}^2$$
$$+ Q_{Rz}^2)^2 + \frac{1}{4}C(Q_{Rx}^2 Q_{Ry}^2 + Q_{Ry}^2 Q_{Rz}^2 + Q_{Rz}^2 Q_{Rx}^2)$$
$$+ \frac{1}{2}D(T - T_M^*)Q_M^2 + \frac{1}{4}EQ_M^4 + \frac{1}{6}FQ_M^6 + \frac{1}{2}GQ_{Rz}^2 Q_M^2$$
$$+ \frac{1}{2}HQ_M^2(Q_{Rx}^2 + Q_{Ry}^2) + \frac{1}{4}IQ_M^2(Q_{Rx}^4 + Q_{Ry}^4)$$
$$+ \frac{1}{2}JQ_M^2 Q_{Rx}^2 Q_{Ry}^2, \tag{1}$$

where F_0 is the free energy of the *Pm3m* structure, Q_{Ri} with $i = x$, y, and z and Q_M are, respectively, the normal coordinates of the R_{25} and M_3 modes, and T is the temperature.[9] Values of T_R^* and T_M^* as well as the coefficient of each free energy term are assumed to be constant. It should be noted that the contribution of the spontaneous strains modifies only the coefficient of each term in an equilibrium condition. In order to avoid complexity, we do not include spontaneous strain terms and coupling terms between the order parameter and the strain in the present free energy expression.

We obtain free energy expressions of the $R\bar{3}c$ and *Pbnm* structures from Eq. (1). Because the main order parameters of the $R\bar{3}c$ structure are given as $Q_{Rx} = Q_{Ry} = Q_{Rz} = (1/\sqrt{3})Q_R$, and $Q_M = 0$, the free energy becomes

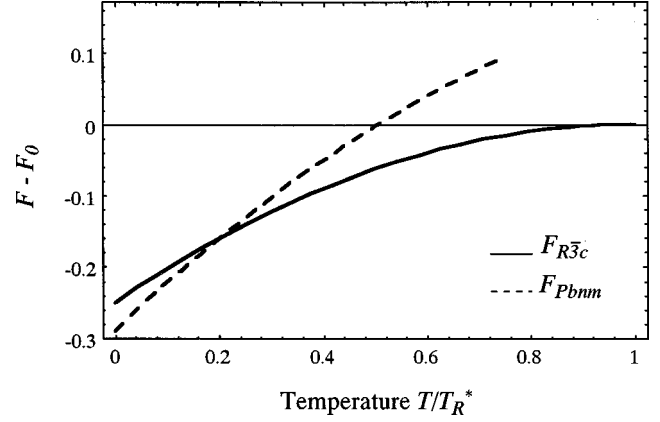$$F_{R\bar{3}c} = F_0 + \frac{1}{2}A(T - T_R^*)Q_R^2 + \frac{1}{4}B_R Q_R^4 \tag{2}$$

FIG. 8. Calculated free-energy curves of the $R\bar{3}c$ and the *Pbnm* phases, represented by solid and dashed lines, respectively.

for the $R\bar{3}c$ structure, where $B_R = B + \frac{1}{3}C$. For the *Pbnm* structure with $Q_{Rx} = Q_{Ry} = (1/\sqrt{2})\overline{Q_R}$, $Q_{Rz} = 0$, and $Q_M \neq 0$, on the other hand, the free energy leads to

$$F_{Pbnm} = F_0 + K_0 + K_1(T - T_R^*) + \frac{1}{2}D(T - \overline{T_M^*})Q_M^2 + \frac{1}{4}EQ_M^4$$
$$+ \frac{1}{6}FQ_M^6, \tag{3}$$

where

$$K_0 = \frac{1}{4}\left(B + \frac{1}{4}C\right)\overline{Q_R^4}, \quad K_1 = \frac{1}{2}A\overline{Q_R^2},$$

$$\text{and} \quad \overline{T_M^*} = T_M^* - \frac{1}{D}\left(H\overline{Q_R^2} + \frac{1}{4}I\overline{Q_R^4} + \frac{1}{4}J\overline{Q_R^4}\right).$$

It should be mentioned that the Q_{Ri} in the *Pbnm* phase is assumed to be a constant value of $(1/\sqrt{2})\overline{Q_R}$ in the present treatment. This is because the $R\bar{3}c$-to-*Pbnm* transition is characterized only by the appearance of the M_3 rotational displacement and the transition temperature of the $R\bar{3}c$-to-*Pbnm* transition must be much lower than that of the *Pm3m*-to-$R\bar{3}c$ one.

Calculated free-energy curves for $R\bar{3}c$ and *Pbnm* phases are shown in Fig. 8. The free-energy terms were calculated up to fourth-order ones, in order to reduce the number of adjustable parameters. Values of A, B_R, D, E, K_0, K_1, T_R^*, and $\overline{T_M^*}$ were actually assumed to be 1, 1, 1, 1, 0.2, 0.4, 1, and 0.6, respectively. It should be noted that the adoption of the terms up to the fourth-order ones does not change the essential features of the $R\bar{3}c$-to-*Pbnm* transition. As is seen in Fig. 8, the free-energy curve of the $R\bar{3}c$ phase intersects that of the *Pbnm* one around $T/T_R^* = 0.2$. This indicates that the present theory can well reproduce the first-order structural transition. It is concluded that the $R\bar{3}c$-to-*Pbnm* structural phase transition is characterized by the intersection of these two free-energy curves. This is a characteristic feature of the typical first-order transitions such as the martensite transition in Fe-Ni alloys.

Finally, we briefly discuss the effect of a magnetic field on the $R\bar{3}c$-to-$Pbnm$ transition. In order to consider this effect, the magnetization vector (M_x, M_y, M_z) is taken into account as a magnetic order parameter. The magnetization vector is obviously an axial vector, which can be transferred by symmetry operations as the basis of the T_{1g} irreducible representation of the O_h point group. As was pointed out by Slonczewski and Thomas,[10] the normal coordinates of the R_{25} displacement, (Q_{Rx}, Q_{Ry}, Q_{Rz}), are also transferred with respect to point-group operations like the components of the axial vector. Therefore there should exist a linear coupling term between them in the free-energy expression. This coupling term would make the free energy lower. It should be noted here that the R_{25}^x, R_{25}^y, and R_{25}^z displacements are involved in the $R\bar{3}c$ structure, while there are only the R_{25}^x and R_{25}^y displacements in the $Pbnm$ structure. Based on this fact, the free-energy gain due to the magnetic field should be larger for the $R\bar{3}c$ phase than for the $Pbnm$ phase. That is, the $R\bar{3}c$ phase is more stabilized by the magnetic field than the $Pbnm$ one. We believe that this stabilization would be a physical origin of the magnetic-field-induced structural phase transition.

V. CONCLUSION

The $R\bar{3}c$-to-$Pbnm$ structural phase transition is characterized by changes in the rotational displacement and in the crystal system. The present study indicated that the former change results in the appearance of the antiphase boundary with respect to the M_3 rotational displacement and that the latter produces the {110} and {112} twin structures. In addition, it was found that the present Landau theory can reproduce the first-order $R\bar{3}c$-to-$Pbnm$ structural transition. It was also noted that a magnetic field has a more stabilizing effect on the $R\bar{3}c$ phase than on the $Pbnm$ phase. The difference in the free-energy gains between the $R\bar{3}c$ and $Pbnm$ phases results in the magnetic-field-induced structural transition.

[1] M. Arao, F. Munakata, and Y. Koyama, Physica C **282–287**, 1111 (1997).

[2] M. Arao, S. Miyazaki, Y. Inoue, and Y. Koyama, in *Proceedings of the 10th International Symposium on Superconductivity (ISS'97)*, edited by K. Osamura and I. Hirabayashi (Springer-Verlag, Tokyo, 1998), p. 219.

[3] A. Urushibara, Y. Moritomo, T. Arima, A. Asamitsu, G. Kido, and Y. Tokura, Phys. Rev. B **51**, 14 103 (1995).

[4] J. B. Torrance, P. Lacorre, A. I. Nazzal, E. J. Ansaldo, and Ch. Niedermayer, Phys. Rev. B **45**, 8209 (1992).

[5] A. Asamitsu, Y. Moritomo, Y. Tomioka, T. Arima, and Y. Tokura, Nature (London) **373**, 407 (1995).

[6] A. Asamitsu, Y. Moritomo, R. Kumai, Y. Tomioka, and Y. Tokura, Phys. Rev. B **54**, 1716 (1996).

[7] D. Louca, T. Egami, E. L. Brosha, H. Röder, and A. R. Bishop, Phys. Rev. B **56**, R8475 (1997).

[8] J. Sapriel, Phys. Rev. B **12**, 5128 (1975).

[9] Y. Fujii, S. Hoshino, Y. Yamada, and G. Shirane, Phys. Rev. B **9**, 4549 (1974).

[10] J. C. Slonczewski and H. Thomas, Phys. Rev. B **1**, 3599 (1970).